Atmos. Chem. Phys., 26, 1931–1946, 2026
https://doi.org/10.5194/acp-26-1931-2026

Atmospheric Chemistry and Physics
Open Access
EGU

Research article

How can we trust TROPOMI based methane emissions estimation: calculating emissions over unidentified source regions

Bo Zheng[1], Jason Blake Cohen[1,2], Lingxiao Lu[1], Wei Hu[1], Pravash Tiwari[1], Simone Lolli[3], Andrea Garzelli[4], Hui Su[5], and Kai Qin[1,2]

[1]School of Environment and Spatial Informatics, China University of Mining and Technology, Xuzhou 221116, China
[2]Shanxi Key Laboratory of Environmental Remote Sensing Applications, China University of Mining and Technology, Xuzhou 221116, China
[3]CNR-Institute of Methodologies for Environmental Analysis (IMAA), Contrada S. Loja, Tito Scalo, 85050, Italy
[4]Department of Information Engineering and Mathematics, University of Siena, 53100 Siena, Italy
[5]Department of Civil and Environmental Engineering, Space Science and Technology Institute, The Hong Kong University of Science and Technology, Clear Water Bay, Hong Kong SAR, China

Correspondence: Jason Blake Cohen (jasonbc@alum.mit.edu, jasonbc@cumt.edu.cn) and Kai Qin (qinkai@cumt.edu.cn)

Received: 26 March 2025 – Discussion started: 10 April 2025
Revised: 20 November 2025 – Accepted: 27 January 2026 – Published: 6 February 2026

Abstract. We propose a novel method for computing the effects of TROPOMI observational uncertainties on emissions calculation arising from the nonlinearity of the gradient terms and non-biased filtering in space and time. Application using TROPOMI X_{CH_4} data in clean areas of Western China with long-term WMO background observations quantifies a minimum detectable emission threshold of 0.3 $\mu g\,m^{-2}\,s^{-1}$, lower than existing community thresholds using TROPOMI. By combining threshold-based and stochastic approaches that incorporates pixel-by-pixel and day-by-day X_{CH_4} uncertainties, we identify and filter physically unrealistic emission values in both space and time. The resulting emissions reveal both missing sources and emission bias caused by the nonlinearity of the gradient term. Validation was performed by applying the method to the Permian Basin, where comparisons with airborne observations demonstrate the method's ability to align with independent datasets. The importance and implications of our results are related to this being a new methodology for methane emissions estimate from TROPOMI which enables precise identification of emission sources and improved handling of observational noise, offering a more accurate framework for methane emission monitoring across diverse regions using existing satellite platforms. Our results yield a non-negative emissions dataset using an objective selection and filtration method, which includes a lower minimum emissions threshold on all grids and reduction of false positives. Finally, the new approach can be adopted to other satellite platforms to provide a more robust and reliable quantification of emissions under data uncertainty that moves beyond traditional plume identification and background subtraction.

Published by Copernicus Publications on behalf of the European Geosciences Union.

1 Introduction

Methane (CH_4) is a potent greenhouse gas with a global warming potential (GWP) estimated to be 28–34 times that of carbon dioxide over a 100 year period and 84–87 times on a 20 year time scale (Hu et al., 2024; Vanselow et al., 2024; Liang et al., 2023). Major sources of methane include fossil fuel extraction, agricultural activities (such as rice paddies and livestock), waste disposal, and wetlands (Vanselow et al., 2024). Since the start of the Industrial Revolution, methane concentrations have been observed to significantly increase (Liang et al., 2023; Erland et al., 2022), with periods of both larger growth and slower or no growth contained within, contributing significantly to the present amount of observed global warming (Vanselow et al., 2024; Erland et al., 2022; Prinn et al., 2001). Due to its relatively shorter atmospheric lifetime compared with many other greenhouse gases, accurately quantifying and controlling methane emissions is crucial in addressing global warming in the near-term (Erland et al., 2022; Liu et al., 2024a).

In recent years, with the development of satellite remote sensing technology, various platforms from space have become more relevant at aiding the monitoring of methane concentrations in the atmosphere (Gao et al., 2023; Nesser et al., 2024). Among them, TROPOspheric Monitoring Instrument (TROPOMI), Greenhouse Gases Observing Satellite (GOSAT) and SCanning Imaging Absorption spectroMeter for Atmospheric CHartoghraphY (SCIAMACHY) have been used for its retrieval of a physical atmospheric CH_4 column retrieval (X_{CH_4}), allowing indirect validation by surface networks (i.e., Advanced Global Atmospheric Gases Experiment (AGAGE) and World Meteorological Organization (WMO)) as well as upward looking surface observational networks (i.e., Total Carbon Column Observing Network (TCCON)) (Hu et al., 2016; Parker et al., 2011; Frankenberg et al., 2005). TROPOMI in particular offers a combination of daily X_{CH_4} retrieval, global coverage, and high spatial resolution (Erland et al., 2022; Liu et al., 2024; Gao et al., 2023; Nesser et al., 2024; Hu et al., 2016). Due to its extensive use to monitor other atmospheric constituents impacting air pollution, there is extensive work to estimate the uncertainty of TROPOMI products including: Nitrogen Dioxide (NO_2) from 10 %–40 % (Boersma et al., 2018; Pollard et al., 2022), black carbon aerosol (BC) from 20 %–50 % (Vignati et al., 2010; Tiwari et al., 2023, 2025), and Carbon Monoxide (CO) starting from a minimum of 10 %–20 % and upwards, without a well-defined upper range (Sha et al., 2021). Additionally, X_{CH_4} from this platform has a significant number of pixels with missing data (Schneising et al., 2023; Qu et al., 2021; Hachmeister et al., 2022; Frankenberg et al., 2016; Hu et al., 2018). Therefore, X_{CH_4} is expected to also have a significant uncertainty, due to at least the following factors: sensor and waveband resolution issues (Hu et al., 2018), atmospheric conditions which reduce the already relatively weak incoming shortwave infrared radiation such as clouds and aerosols (Balasus et al., 2023; Liu et al., 2024b; Liu et al., 2024b), and surface reflectivity (Balasus et al., 2023).

Computing emissions from concentration requires an additional step that includes knowledge of the wind, atmospheric transport and diffusion, in-situ processing and other processes (Cohen and Prinn 2011; Cohen et al., 2011). There are many studies which have used various complex approaches such as chemical transport models (Hancock et al., 2025; Nesser et al., 2024; Varon et al., 2023) and simple approaches such as the Gaussian integral method (Schneising et al., 2020), Divergence method (Liu et al., 2021; Veefkind et al., 2023), mass balance method (Hu et al., 2024) to attempt to estimate methane emissions from TROPOMI in near real time. However, due to the uncertainties in the retrieved TROPOMI data and wind fields, the computation of gradient term(s) necessary to compute emissions may lead to significant non-linearity (Cohen and Prinn 2011; Cohen et al., 2011; He et al., 2024), thereby generating negative emissions and smaller emission values. Hancock et al. (2025) prevented non-physical negative emissions by inverting prior emissions using the lognormal error probability density function (PDFS), Schneising et al. (2020) defined the background from a $2° \times 4°$ headwind box and determined negative emissions or very low emissions for many days in the Permian basin, despite strict filtering criteria for background observations. Veefkind et al. (2023) employed background subtraction to filter out negative emissions and smaller emission signals in Permian basin and believed that the intense variations in topography and surface albedo may lead to significant negative emissions. However, these studies did not further analyze the causes of negative emissions. Simple background filtering methods cannot effectively remove all emission noise, and may in fact leave noise contributing to overestimation of actual emissions. Therefore, finding ways to address how observed and modeled uncertainties lead to the robustness of inverted methane emissions is a necessary and essential step to gain trust in resulting emission quantification and usefulness for attribution (Li et al., 2023, 2025; Tiwari et al., 2025). To gain confidence, such emissions should include methods which are both unbiased and robust, and are capable of identifying sources both known and unknown, monitoring emissions from those sources, and provide validation of which sources are actually being reduced or eliminated (Hemati et al., 2024).

In this study, we quantify CH_4 emissions in a clean area with a long-term WMO observational station (Waliguan) using a flexible mass-conserving method that explicitly accounts for the impacts of X_{CH_4} observational uncertainties on the gradient terms and their influence on emission inversion. Selecting a region devoid of large emission sources is critical, as it allows for an objective demonstration of the effects of white noise generated by the nonlinearity of the gradient term on emission calculations. To address this, we introduce unbiased thresholds and filters to systematically separate genuine emission signals from white noise, effec-

tively eliminating physically implausible emission values in an unbiased manner. Our results demonstrate that all identified emissions correspond to spatial and temporal locations where emissions are expected to occur, with no computed emissions detected in regions where emissions should not exist. To further validate the robustness and applicability of our method, we applied it to the Permian Basin, the largest and fastest-growing oil and gas-producing basin in the United States, located in western Texas and southeastern New Mexico. By aligning our results with known emission source locations in the region, we successfully captured the majority of emission signals, including many smaller emissions that were previously undetected using TROPOMI, thanks to our method's lower detection threshold. Comparisons with conventional approaches, which simply remove negative concentration or emission values, reveal that our method provides a better match with observational data, demonstrating improved stability, accuracy, and a reduction in systematic bias. This highlights that this approach is capable of delivering reliable and precise emission estimates, even in areas with complex sources.

2 Data and Methods

2.1 Study regions and data

Waliguan was selected due to its long-term daily surface observation dataset of CH_4 from 1992 through 2024 (Zhou et al., 2004; Liu et al., 2021). Waliguan is the world's highest atmospheric baseline monitoring station (at 3810 m), as well as being far from all coasts, and therefore is a representation of a clean, continental, high atmospheric station in mid-latitudes. Critically, it offers a good representation of middle atmospheric CH_4 levels, which also makes it the only background site which is representative of the outsized number of coal mines with high emissions from Shanxi, Shaanxi, Inner Mongolia, Xinjiang, which are also located at high elevations and far away from the sea (Yang et al., 2023; Zhang et al., 2020). It is further representative of the conditions under which CH_4 is emitted in other lesser studied regions around the world (Sadavarte et al., 2021; Hancock et al., 2025).

The Permian Basin, situated in western Texas and southeastern New Mexico, is the largest and fastest-growing oil and gas-producing basin in the United States, with oil and natural gas production in the Permian Basin surged from 2014–2019 (EIA) and by 2020 represented 38 % of total US oil production and 17 % of total US natural gas production. We validate the applicability and robustness of our method by comparing our results over this region with airborne observations made by Cusworth et al. (2021).

TROPOMI inverts daily measurements of column-averaged dry-air atmospheric CH_4 column mixing ratio based on a retrieval around the NIR and SWIR absorption bands, with overpasses occurring daily around 13:30 local time. The X_{CH_4} retrieval used herein (version 2.4.0 Level-2) relies on a physical algorithm that factors in surface and atmospheric scattering. In this study, we use the methane total column-averaged dry-air mole fraction X_{CH_4} of TROPOMI from May 2018–December 2023 in Waliguan (35.5–37.1° N latitude, 100.1–101.7° E longitude) (Hu et al., 2018; Lorente et al., 2021; Landgraf et al., 2024) and from 2019–2020 in the Permian Basin (31–33° N latitude, 101.3–104.3° W longitude). To ensure high quality data, grids with quality assurance less than 0.5 were removed. Swath-by-swath data were resampled day-by-day onto a standard latitude/longitude grid of $0.05° \times 0.05°$ using Harmonization and Analysis of Remote sensing data Package (HARP) (http://stcorp.github.io/harp/doc/html/index.html).

Wind speed and direction were obtained from the European Centre for Medium-Range Weather Forecasts ERA-5 reanalysis product. Due to the elevation and overpass time, 550–750 hPa level meteorology products were used in the Waliguan area and 750–950 hPa range products in the Permian Basin, both using an average value based on of local 13:00 and 14:00 UTC (Hersbach et al., 2023).

Daily ground observations of CH_4 made for more than three decades at Waliguan are obtained from World Data Centre for Greenhouse Gases. The source coordinates and emission rates of methane in the Permian Basin were obtained from an aircraft observational study by Cusworth et al. (2021).

High frequency CH_4 flux was measured nearby a gas extraction vent of a high gas coal mine in Changzhi, Shanxi Province using the eddy correlation method, using CSAT-3 anemometer and LI-7700 and Universal open Path gas analyzer at 10 Hz as published in Hu et al. (2024). The flux was calculated according to the WPL-corrected method (Webb et al., 1980) and subsequently narrowed down to a frequency of every half hour. Observations were made continuously from 24 October–21 December 2021 and from 15 August–13 September 2022. The flux observations obtained from eddy covariance observations are specifically used to fit the coefficients of the mass conservation model at the date and time they are available, providing a ground-truth at the place and time the observations were made.

2.2 Mass conservation equation

The method used in this study is based on the continuity equation for conservation of mass of chemical substances in the atmosphere.

$$E = \frac{\mathrm{d}}{\mathrm{d}t} X_{CH_4} + H + D + T \tag{1}$$

where E is the emission flux, $\mathrm{d}/\mathrm{d}t\, X_{CH_4}$ is the time derivative of X_{CH_4}, H is the chemical gain or loss of CH_4, D is the deposition of CH_4, and T is the transport gain or loss of CH_4 on each given grid in space and time. Due to the slow nature of CH_4 loss induced by OH, its low solubility, and its slow removal due to other oxidants and bacteria as compared to

the daily-scale observations used herein, the terms for chemical gain H and deposition D in Eq. (1) are approximately zero, allowing Eq. (1) to be simplified as:

$$\begin{aligned}\frac{\mathrm{d}}{\mathrm{d}t}X_{\mathrm{CH_4}} &= E - T \\ &= E - \alpha \times (\nabla \cdot (X_{\mathrm{CH_4}} \times U)) - \beta \times \nabla \cdot (\nabla X_{\mathrm{CH_4}})\end{aligned} \tag{2}$$

The transport term T is approximated by the combination of advection and pressure induced transport $\nabla \cdot (X_{\mathrm{CH_4}} \times U)$ ($\times$: multiplication sign) and diffusion $\nabla \cdot (\nabla X_{\mathrm{CH_4}})$, where U is wind field. We specifically use the methane flux measured at Changzhi as E and calculate the time derivative, transport, and diffusion terms for the corresponding position and time over Changzhi. The coefficients α and β are then calculated using Multiple Linear Regression. The resulting emissions have been previously demonstrated to work well in Shanxi (Hu et al., 2024). In this work, the trained model is used to calculate emissions across all grids on all days where there is sufficient available TROPOMI and meteorological data to compute all of the terms. The uncertainty range of emissions is determined by the range from the 20th percentile to the 80th percentile of the emission values obtained through multiple sets of coefficients.

2.3 Observational Uncertainty Analysis

Our model and other more simplified approaches (Cohen and Prinn 2011; Liu et al., 2021; Yu et al., 2023) rely upon concentration gradients, such as the transport term and diffusion term in our equations and the divergence method used by others (Liu et al., 2021; Veefkind et al., 2023) , when considering a certain volume of air, we can calculate the number of CH_4 molecules flowing into and out of that volume based on column density and representative wind speed and direction acting upon that atmospheric column. Under steady state conditions, a positive difference indicates the presence of a CH_4 emission source. However, the value of a gradient does not linearly vary with the uncertainty in the observations. For instance, if the $X_{\mathrm{CH_4}}$ values at two adjacent grid points are 1800 and 1900 ppb, with a 10 % uncertainty, they can range from 1620–1980 and 1710–2190 ppb respectively, leading to a possibility that the gradients could range from negative, to zero, or even moderately positive. Sinks comprise chemical losses, such as reaction with the hydroxyl radical, OH, and atomic chlorine and biological losses, primarily uptake by methanotrophic microbes in soil. The lifetime with respect to reaction with OH in the troposphere is between 10 and 11 years and the average lifetime of methane in the atmosphere is 9 years, methanotrophic bacteria achieved methane oxidation rates of about 5.6 $\mathrm{nmol\,cm^{-3}\,d^{-1}}$. Forest soils that cover about 30 % of the Earth's land surface absorb about 26–34 Tg CH_4 per year. However, we calculated TROPOMI $X_{\mathrm{CH_4}}$ data day by day, grid by grid, and the two cases have little effect on methane concentration. Hence, there is no physical means by which a negative lifetime can occur in our framework. Therefore, only white noise generated by the nonlinearity of the concentration gradient is possible to achieve negative emissions.

However, merely removing negative values is not mathematically consistent with white noise, due to the randomness of the uncertainties applied to the observed data being equally likely to be positive or negative. Therefore, any values which fall in the probability distribution which is best fit by a normal distribution with a center at zero, are associated with this noise. They are computed values, but are just due to the noise associated with the observational uncertainty. It is essential to compute how these uncertainties impact the real conditions when considering the spatial change in the observed fields. This includes not only the observed values themselves, but also whether or not the underlying assumptions of the model used are still relevant, or whether the simple idea of a plume model may still be possible. For example, if the gradient switches direction when uncertainty is applied, the chances of the plume being real are significantly reduced, with the original detected plume more likely being just noise, rather than a real signal.

To analyze this effect, we use the mass conservation equation to quantify methane emissions in the area around the Waliguan (WLG) long-term base station, because there are no large known sources of methane emissions in this area, the effect of noise due to the non-linearity of the gradient term can be better demonstrated, with most recent studies computing emissions using background subtraction (Schneising et al., 2020; Liu et al., 2021; Veefkind et al., 2023) which instead of computing actual emissions rather computes a signal based on observational noise in both the background value and the enhancement value in addition to the effects of any actual emissions. Instead, this work subsequently uses the entire column loading $X_{\mathrm{CH_4}}$ and applies two different magnitudes of random perturbations to the observations: 10 % and 20 %. In each case, a respective value ranging from -10 % to $+10$ % (or 20 % respectively) is made independently to each TROPOMI retrieved $X_{\mathrm{CH_4}}$ data point, day-by-day, and grid-by-grid to simulate realistic and unbiased TROPOMI retrieval errors. 1000 unique sets of perturbations have been performed. Each of these 1000 data sets have been used to retrain the emissions via Eq. (2), with the resulting average value grid-by-grid and day-by-day used.

2.4 Threshold retrieval

To identify potential emission sources in the study area and separate these from white noise, we take a two-step approach.

1. Spatial filtering: we filter all grids in terms of their mean value, with any grids having temporal average emissions values smaller than the 65th percentile of emissions (in this case 26.5 $\mathrm{\mu g\,m^{-2}\,s^{-1}}$) removed, to account for the fact that these grids likely are contributed to exclusively by white noise. Sensitivity tests are performed

using different cutoff values for the first cutoff, specifically the 50th percentile of emissions ($12.4\,\mu g\,m^{-2}\,s^{-1}$), and re-computing the resulting emissions each time using all of the TROPOMI uncertainty levels as used elsewhere.

2. Temporal filtering: the idea is extended to the temporal domain, considering the seasonal variations in emissions (Varon et al., 2025), we conduct monthly filtration, specifically assuming that any negative emissions values must be due to observational uncertainty, and therefore any positive value of the same magnitude or smaller on that same grid is also due to uncertainty. Specifically, within each remaining grid point, the most negative emission value computed is identified $-\theta\,\mu g\,m^{-2}\,s^{-1}$ (θ: the absolute value of the minimum negative emission in the grid), and all values in the range from $[-\theta : \theta]\,\mu g\,m^{-2}\,s^{-1}$ are then excluded. This filter is applied grid-by-grid basis, since the uncertainty is assumed to be an intrinsic property of each grid point, consistent with how the retrievals are computed.

3 Results and discussion

3.1 Observation error

Due to the following factors, retrievals of CH_4 from TROPOMI may have relatively large uncertainties in some regions (noting that their influence varies as a function of location and time). First, when there is overlap between CH_4 and other species which are not resolved (i.e., waveband resolution of the sensor). Second, when atmospheric conditions reduce incoming solar radiation in the wavebands relevant to CH_4 retrieval (i.e., cloud optical depth and AOD). Third, when atmospheric conditions alter the band-by-band properties of incoming and scattered solar radiation in the wavebands relevant to CH_4 (i.e., BC and CO). Fourth, when changes in the land-surface properties have occurred which are not properly modeled or included, such as due to development, greening, industrial growth, agriculture changes, etc. (i.e., changes in surface reflectivity).

The uncertainty of the aerosol products of TROPOMI is 3 %–5 % (Torres et al., 2020; Tiwari et al., 2023). As a first order problem, no gas retrievals can be performed until the surface albedo, clouds, and aerosols are first considered (Balasus et al., 2023), or the combination is considered in tandem (Chen et al., 2022). In addition to this point, it has been demonstrated that TROPOMI L2 X_{CH_4} retrievals are routinely underestimated over regions with high aerosol loadings (Li et al., 2024). Therefore, since the region considered has a variable AOD, and one which is quite different from the traditional datasets employed to initiate the inversion algorithm (Liu et al., 2024b), therefore this factor must also be considered in the area being analyzed. For this reason alone, it is not possible for the CH_4 retrieval to have an uncertainty lower than the aerosol retrieval uncertainty. TROPOMI NO_2 has an error range from 10 %–40 % or more (Boersma et al., 2018; Pollard et al., 2022). It is also known that TROPOMI CO has an error range of at least 10 % to 20 % (Sha et al., 2021). The uncertainties in the traditional datasets employed with respect to CO over China are significant (Li et al., 2025; Wang et al., 2025). This is important since the CO retrieval is made at the same waveband as the CH_4 retrieval, and therefore any uncertainty in one product will yield an uncertainty in the other product as previously identified (Gaubert et al., 2016, 2017).

A direct comparison between the surface observations of Waliguan and the TROPOMI X_{CH_4} column concentration, as clearly observed in Fig. 1b, demonstrates a difference up to 176 ppb, or a 9.4 % error. Observed vertical CH_4 profiles were made by Tao et al. (2024). Figure 2 in Tao et al. (2024) using AirCore at the same time and very close to where this work's satellite observations were analyzed. The results compare closely with the surface observations made at the WMO station in Waliguan, validating that the surface observations in this region are a reasonable representation of the column average values, as shown in Fig. 1. Based on this, we add a random perturbation to each retrieved value of TROPOMI X_{CH_4} in the range from −10 %–10 % to simulate the uncertainty in the retrieval data itself. This is also consistent with the observational study of Frankenberg et al. (2016), indicating that the observed error can range over 20 %.

3.2 Comparison of emissions before and after application of filtration in Waliguan area

As illustrated in Fig. 2, the distribution of computed emission over all pixels on all days exhibits a predominantly normal distribution pattern, and therefore closely resembling the distribution of white noise. Upon closer inspection, the distribution reveals obvious positive bias, signifying the presence of mixture of genuine subset of emissions values which are computed not due to the observational uncertainty contained within the overall set of computed emissions data. The distribution derived without employing the two-step filtering process, but incorporating a 10 % TROPOMI uncertainty, shows only marginal deviations from the original emissions.

Figure 3a highlights a significant occurrence of near-zero or negative emissions in spatial regions where no emission sources are expected, suggesting the presence of numerous false positives. To address this, a probability density function (PDF) threshold is established based on the point where the distribution deviates from normality on the positive side. Grids with mean emissions exceeding this threshold are retained to distinguish potential real emissions from noise-dominated grids. An example of such a grid, marked by a black box in Fig. 3a, demonstrates a mean emission value surpassing the threshold.

Following this initial spatial filtration, a secondary temporal filtering step is applied to the remaining pixels, Fig. 3b

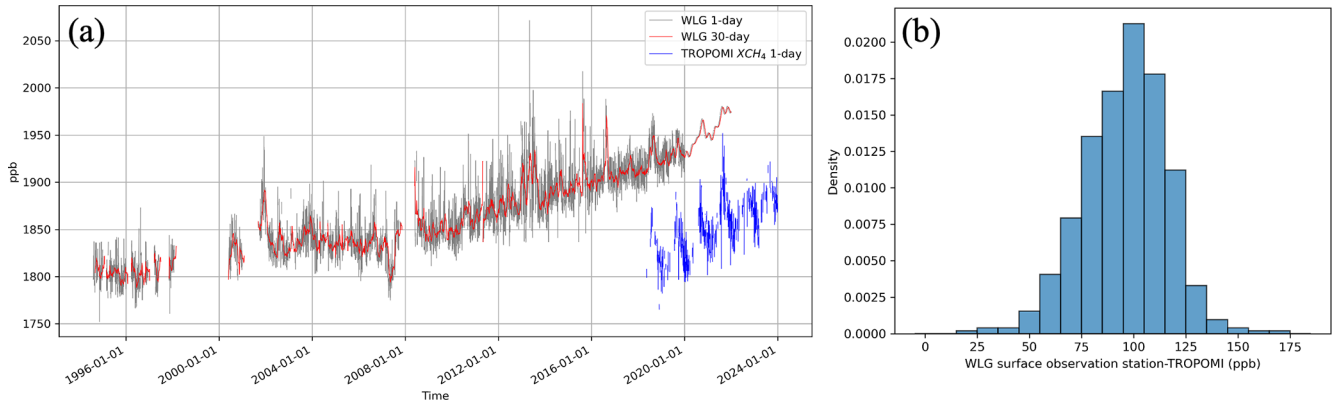

Figure 1. **(a)** Daily (grey) and 30 d mean (red) methane concentration data from Waliguan from August 1994–December 2021 and daily series of TROPOMI X_{CH_4} (blue) from April 2018–December 2023; **(b)** The difference between Waliguan daily methane concentration and TROPOMI X_{CH_4}.

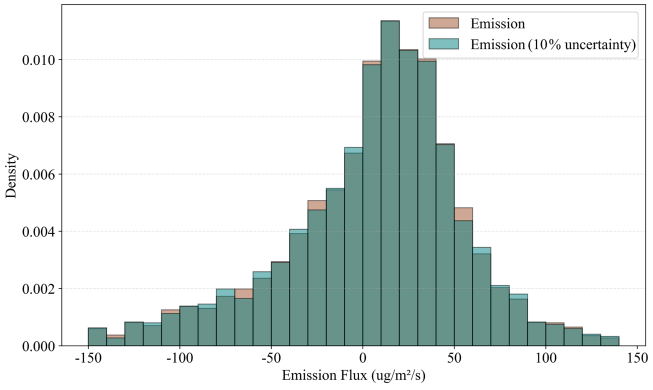

Figure 2. PDF of methane emissions from the Waliguan region calculated using TROPOMI X_{CH_4} and X_{CH_4} ±10 % based on the mass conservation model.

and c show the time series before and after filtering by the red grid in Fig. 3a. This step effectively eliminates unphysical values and those arising solely from observational noise, ensuring that only robust emission estimates are considered for further analysis.

The spatial distribution of day-to-day and grid-to-grid emissions over five years is presented in Fig. 4a–c (pre-filtering) and Fig. 4d–f (post-filtering). Negative emissions are mainly concentrated in areas A and C of Fig. 4a. The point of the filtering is to determine whether or not observational uncertainty or noise was the source of the retrieved emissions, or if the retrieved emissions were due to a physical signal. Some physical factors which contribute to signal observational uncertainty or noise which still exist in the QA > 0.5 data include but do not fully filter for thin clouds and aerosol layers as well as moderate variations in water vapor, or medium-low albedo (Hu et al., 2016). This QA level also does not consider aerosol absorption or apply any constraints on co-absorbing gasses including but not limited to carbon monoxide. However, this work specifically analyzed a some of these drivers, and clearly determined that some of these drivers in fact contributed to those grids which were filtered (i.e., areas in which the emission derived from the signal were negative or sufficiently small or large and positive to be considered noise).

Aerosols impact X_{CH_4} in two different ways, through scattering and through absorption. First, aerosols increase radiative scattering, changing the entirety of the stream of energy (Kahn et al., 2023; Liu et al., 2024b; Tiwari et al., 2023, 2025), while also absorbing radiation, affecting line-by-line radiance absorption used to invert X_{CH_4} based on Beer's Law, DOAS, or similar physics-based techniques (Kuhlmann et al., 2025; Tian et al., 2021; Guan et al., 2025). We have included observations of AOD at a band as close to that retrieved from TROPOMI as possible (specifically observed by MISR at 865 nm). As shown in Fig. S1h in the Supplement, almost all of our valid emissions occur at locations where the 2019–2021 average AOD is less than 0.3. Figure 5b and e show the PDFs of AOD corresponding to the points in space and time of the invalid and valid emissions, respectively, while spatial plots (see Fig. S2b and e) detail that while all grids are low, that those grids with valid emissions have lower AOD than grids with invalid emissions. Furthermore, we have analyzed the TROPOMI AOD_SWIR product (Fig. S2), and found similarly that where our emissions are valid, the AOD remains both very low, as well as being smaller than the AOD on the invalid emissions locations, as show in Fig. S2a and b.

Next, we examine the impact of aerosol absorption based on MISR AAOD at 443 nm, 865 nm, and the ratio of the two AAODs as given in (Fig. S1e, f, g) following Liu et al. (2026). Areas with a large AAOD ratio indicate the presence of larger-sized absorbing aerosol, which is more likely to impact the radiation wavebands used in the inversion of X_{CH_4}. We observe that the ratio is somewhat larger over areas with

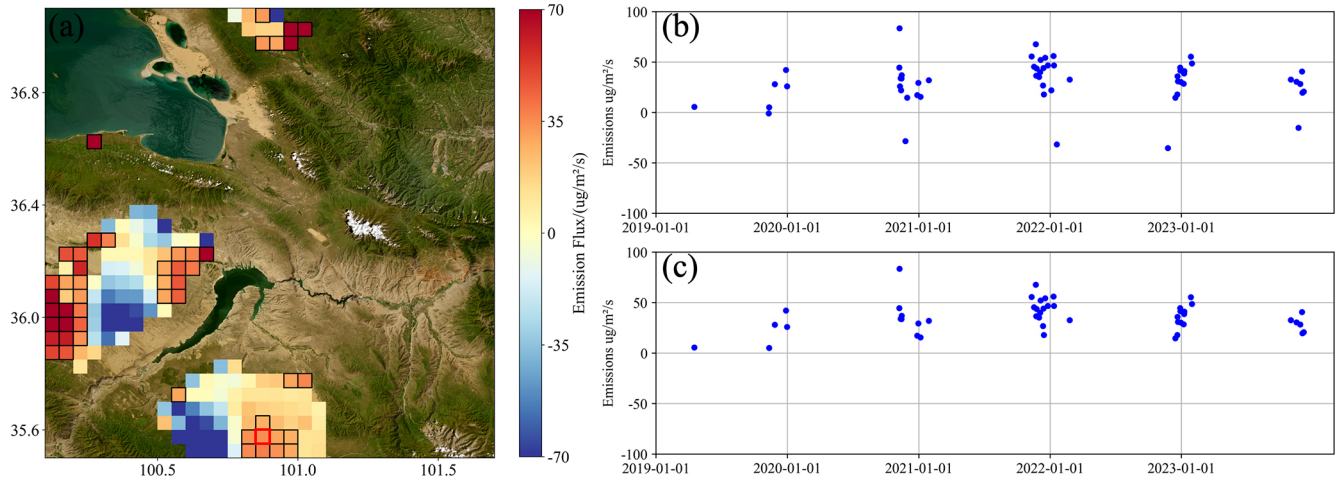

Figure 3. **(a)** Five-year emission mean calculated by TROPOMI X_{CH_4}, the mean of the grids in the black boxes are greater than the set threshold ($12.4\,\mu g\,m^{-2}\,s^{-1}$) (background portion of image is from Esri World Imagery | Powered by Esri); **(b, c)** are the unfiltered and filtered emission time series of the red grid in **(a)**.

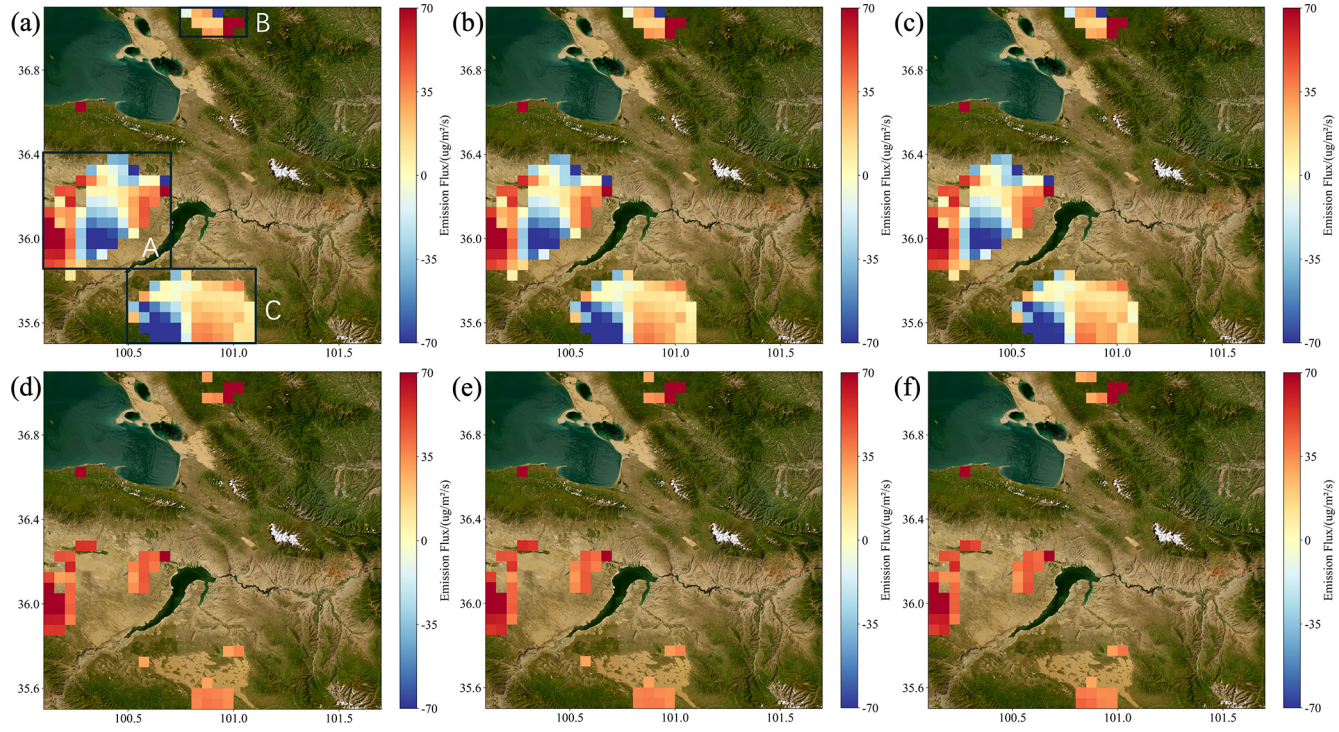

Figure 4. **(a–c)** are maps of five-year emission averages calculated using TROPOMI X_{CH_4}, X_{CH_4} ±10 %, and X_{CH_4} ±20 % respectively; **(d–f)** are maps of the five-year emission average obtained after the two-step filtering is applied corresponding to **(a–c)**. All backgrounds are from Esri World Imagery | Powered by Esri.

emissions we have filtered (such as area A in Fig. 4a). Furthermore, we observe that most of the grids with valid emissions are located are in areas with very low AAOD ratios. The PDFs of the AAOD ratio for the invalid and valid emission points, shown in Fig. 5a and d respectively. Therefore, our approach is successful in determining that the pixels more impacted by aerosols are in fact filtered.

The surface albedo in this region as shown in Fig. S1d. Our retained emissions do not occur at locations with either very low or very high surface albedo. Moreover, compared with the retained emissions (Fig. 5c and f), the surface albedo corresponding to the filtered emissions are typically found closer to the extreme ends of the albedo range.

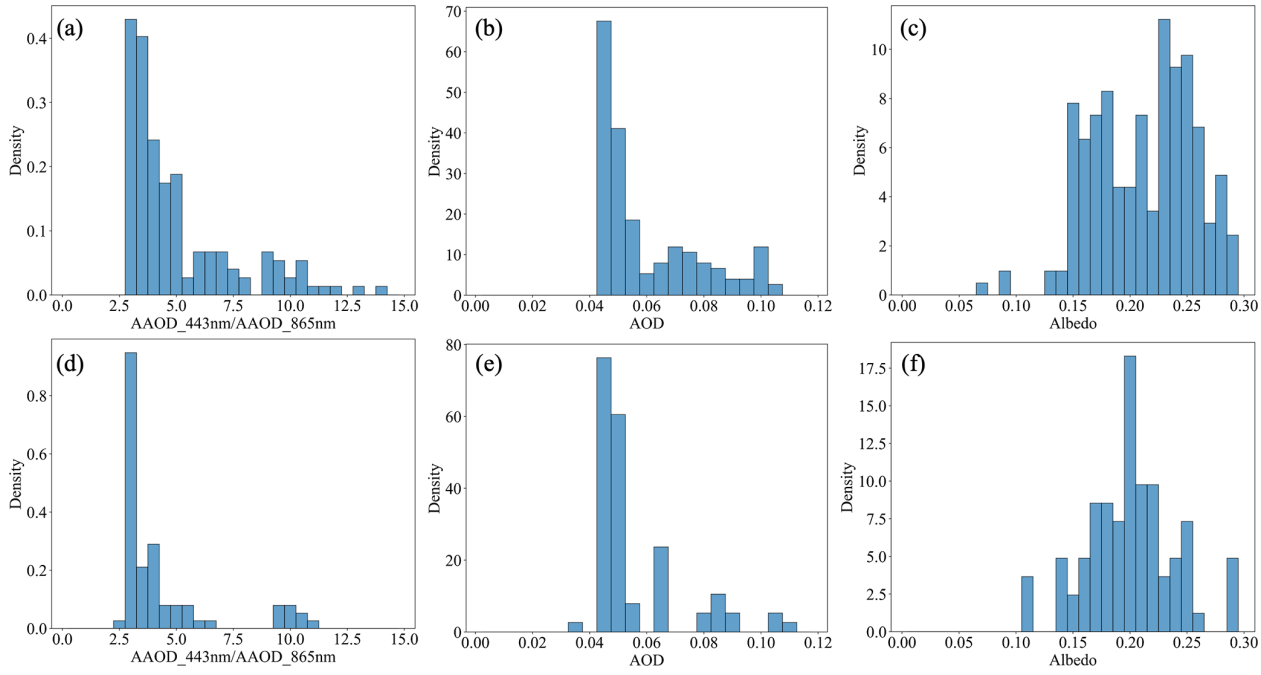

Figure 5. **(a)–(c)** are the PDFs of the ratio of MISR AAOD observed at 443 nm to AAOD observed at 865 nm, MISR AOD observed at 865 nm, and albedo corresponding to the location of the filtered emission (invalid emissions), respectively; while **(d)–(f)** are the same respective values, but corresponding to the location of the retained emissions (valid emissions), respectively.

These factors alone cannot explain the total uncertainty, which may be influenced by other parameters, such as cloud, sensor, water vapor absorption, carbon monoxide and waveband resolution issues, etc. This result offers a physical explanation of why there is a substantial uncertainty in the X_{CH_4} retrieved values. What is also important is that our approach is capable of detecting such a non-linear uncertainty propagation, while standard emissions estimation approaches (Schneising et al., 2020; Veefkind et al., 2023; Hancock et al., 2025) in fact compute negative emissions, without realizing that the emissions are merely due to observational uncertainty. To be clear, this approach herein is further validated, since applying the uncertainty in general does actually capture a subset of physical driving factors which are expected to lead to greater retrieval noise.

A comparison of the filtered emissions in Fig. 4d with the actual geographical map reveals that the filtered results accurately capture known emission sources: towns and villages. The emission time series (Fig. S3) in regions A, B and C show that emissions are mainly concentrated around the Spring Festival, which is consistent with the increase in methane emissions caused by the short-term influx of people and increase in human activities during this period. However, these small-scale anthropogenic sources are omitted in existing emission inventories over this region (Crippa et al., 2024). Our filtering method effectively removes noise, retaining only grid points corresponding to plausible emission sources. All grid points identified as emissions in this study are scientifically justifiable, whereas many grid points initially classified as white noise (Fig. 4a) lack any known anthropogenic or natural emission sources substantial enough to have an emission corresponding to the lowest calculated value herein.

The distributions in Fig. 4b, e and c, f correspond to the 10 % and 20 % TROPOMI uncertainty scenarios, respectively. These distributions largely overlap with the results shown in Fig. 4a and d. Specifically, when the TROPOMI X_{CH_4} data incorporates a 10 % error, the filtered grid points align closely with the original emissions, with only a single grid discrepancy. This demonstrates the efficacy of our method in filtering out noise induced by the nonlinearity of the gradient term. However, when the TROPOMI error is increased to 20 %, the robustness of the filtering method slightly diminishes. When the 50th percentile emission value ($12.4\,\mu g\,m^{-2}\,s^{-1}$) of the emission result was used as the threshold for mean filtering in the first step of filtration (Fig. S4), the grid discrepancy in regions A and B was not obvious, but emissions occurred in the desert area of region C, this indicates the necessity of the first step of spatial filtering. Overall, Eq. (2) successfully conserves mass by balancing the nonlinearity in the gradient terms through the contributions of other terms, ensuring reliable and consistent results.

Scatter plots in Fig. 6a and b compare the emissions of 0 % TROPOMI uncertainty with those of 10 % TROPOMI uncertainty and 20 % TROPOMI uncertainty respectively, with the respective R^2 and RMSE being 0.99, 3.41 and 0.98,

6.81. The unfiltered emissions contain points which may be mathematically correct, but physically unreasonable including points with a roughly zero mean and substantial noise, or random extreme values. The results after two-step filtering are given respectively in Fig. 6c and d, and have respective R^2, RMSE of 0.99, 3.7, and 0.95, 7.37. Although the number of emissions after filtering in Fig. 6c and d decreased by 70 % compared to Fig. 6a and b, R^2 was similar at 10 % TROPOMI uncertainty case, with RMSE increasing by 0.29, and a slight reduction in the R^2 in the 20 % TROPOMI uncertainty case, with RMSE increasing by 0.56, which actually indicate that overfitting is less of an issue, consistent with the fact that the observations contain actual uncertainty.

The range of filtered emissions assuming 0 %, 10 %, and 20 % TROPOMI uncertainty bounds respectively are 0.3–187, 0.2–187, and 0.5–195 $\mu g\,m^{-2}\,s^{-1}$. In all cases applying the methods herein led to all negative values (unphysical) being filtered, as well as the largest positive values also being filtered. This is consistent with the fact that some very high observed values are also noise, and that the process herein in fact applies an unbiased and reasonable result. These discrepancies in the mean values arise because the first and second order gradient terms both behave non-linearly when observational uncertainties are included. The fact that the linear terms and the temporal derivative are able to buffer the non-linearity allows the resulting emissions to be robust, and requires that emissions calculations must include these terms to be stable.

Many studies after calculating emission either use an absolute value of the gradient or simply remove negative resulting values, either way retaining only positive results (Veefkind et al., 2023; Liu et al., 2021). We have performed the same analysis approach and show the results in Fig. 6e and f to compare the base emissions results against the 10 % and 20 % TROPOMI uncertainty cases respectively. This method results in emissions that include a large amount of noise both near zero as well as some extremely high values at the top. Furthermore, it is found that these extremely high and nearly zero values occur in locations without any known emissions sources. This increase in near-zero noise leads to genuine small emissions sources being indistinguishable from noise, resulting in a lower average emissions per grid, and a far larger number of grids than is realistic.

3.3 Methane emissions of the Permian Basin

The emission estimated in the Permian Basin without considering satellite uncertainty is shown in Fig. 7a, negative and near-zero values appear in certain areas, with similar results observed when applying divergence-based methods to quantify emissions in this region using TROPOMI with both plume-based methods (Veefkind et al., 2023) and Gaussian integral method (Schneising et al., 2020). The unfiltered computation of grid-by-grid and day-by-day emissions exhibits a significant positive shift compared to Waliguan, a reasonable outcome given the presence of genuine and substantial emission signals, Interestingly, the overall result still contains a large amount of data centered around 0, as evident in Fig. 7b. As previously demonstrated, traditional methods that simply remove negative values or employ background subtraction retain substantial noise near zero as well as some maxima, leading to artificially low emission estimates.

The results after applying our two-step filtration method are presented in Fig. 7c. Post filtration, the mean emission values have increased significantly compared to the pre-filtration values, with all negative values and noise near zero effectively removed. The quantified true emissions range from 0.5–210 $\mu g\,m^{-2}\,s^{-1}$, with the range of values slightly lower than but overlapping with results from other studies such as from high gas coal mining areas in Shanxi China (Hu et al., 2024; Qin et al., 2023). Notably, unlike background subtraction, our filtering method does not indiscriminately remove all values below a predetermined threshold. As illustrated in Fig. 7d, the minimum emission value detected after filtering is 0.5 $\mu g\,m^{-2}\,s^{-1}$, consistent with the smallest detectable signal of 0.2–0.3 $\mu g\,m^{-2}\,s^{-1}$ observed in the Waliguan region, demonstrating the capability of our method to identify small emission signals.

To better compare with other inventories many of which use emissions in terms of mass per time per grid, we first convert emissions fluxes ($\mu g\,m^{-2}\,s^{-1}$) into emission rates over each entire TROPOMI grid ($kg\,h^{-1}\,grid^{-1}$). The EDGAR emission inventory over the Permian Basin is shown in Fig. S6a, and Fig. S6b shows the difference between our emission results and EDGAR, with the grid-by-grid ranging from $-285 - 3830\,kg\,h^{-1}\,grid^{-1}$, and the 95th percentiles of the difference is $2920\,kg\,h^{-1}\,grid^{-1}$. The EDGAR emission inventory is significantly lower than our results, in part due to many emissions grids missing from their dataset, although their grid with the highest emission is still lower than our result, indicating that our approach does not have a high bias. We also compared the differences between the inventory of Cusworth et al. (2021) and EDGAR, as shown in Fig. S6c. The difference range is from -3240–$8440\,kg\,h^{-1}\,grid^{-1}$, and the 95th percentiles of the difference is $2450\,kg\,h^{-1}\,grid^{-1}$, which is close to the difference range between our results and EDGAR.

Cusworth et al. (2021) measured the emission rates of individual sources, and due to the intermittent nature of the aircraft observations, the number of days with detectable emissions varied from 0–12 d for each source, with the vast majority having only 1 or 2 d of data. When multiple emission sources were located within a single grid, their emission rates were summed to represent the total emission rate of that grid (Fig. S7). Figure 8a shows our filtered emission mean, overlapping with the grid of ground emission sources. It's clear that our results are larger, which is consistent with the observations made by aircraft having scan widths of 3 and 4.5 km, which is always smaller than our grid resolution of 0.05 by 0.05, which is about 5 km. This means that even if their scan

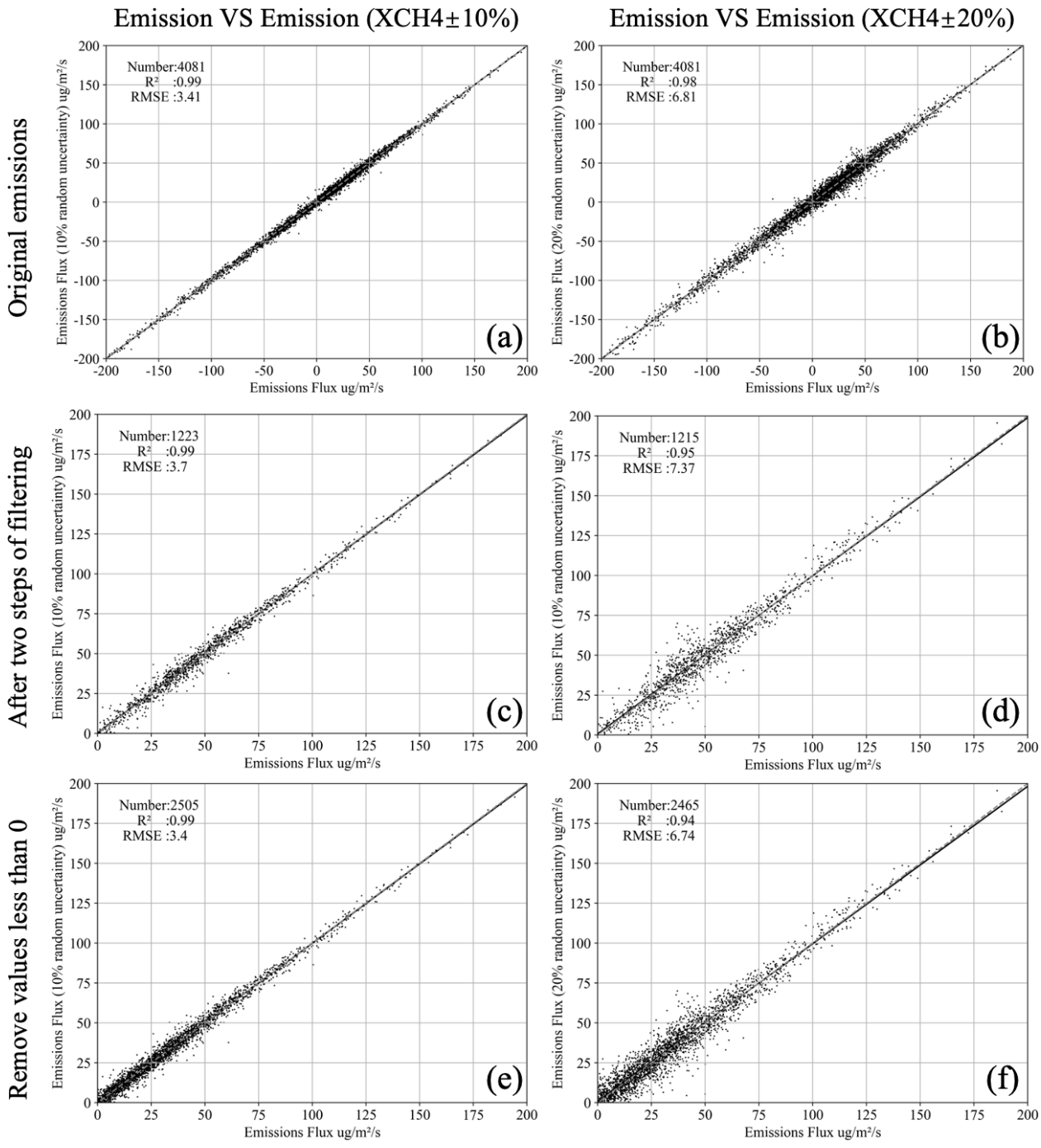

Figure 6. **(a, c, e)** Scatter plots representing each computed emissions value in terms of grid-by-grid and day-by-day from TROPOMI X_{CH_4} (x axis) and TROPOMI X_{CH_4} $\pm 10\,\%$ (y axis); **(b)**, **(d)**, **(f)** are as **(a)**, **(c)**, **(e)** respectively, but where the y axis is TROPOMI X_{CH_4} $\pm 20\,\%$. Plots **(a)**, **(b)** contain all computed emissions before any filtration. Plots **(c)**, **(d)** show the results after both thresholds are applied. Plots **(e)**, **(f)** apply the traditional method of removing all computed emissions lower than $0\,\mu g\,m^{-2}\,s^{-1}$.

crossed the center of our grid, our grid would still contain information outside of their scan width, and if the scan only crossed a small amount of our grid, then the grid would contain far more information.

The red dots in the scatter plot of Fig. 8b represent the points where our emission results overlap with Cusworth et al. (2021) in both time and space, with $R = 0.8$ and MAE $= 660\,kg\,h^{-1}\,grid^{-1}$, both indicating a reasonable agreement. The black dots and blue dots respectively repre-

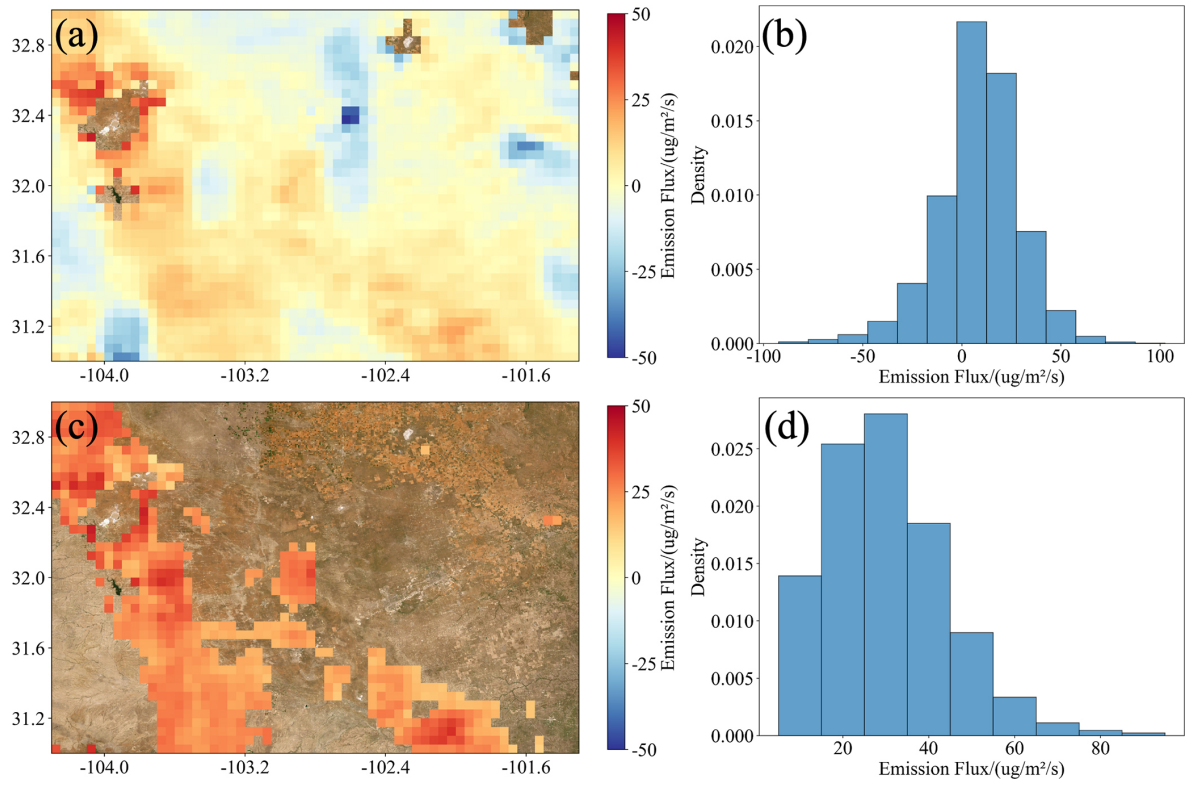

Figure 7. **(a)** Annual mean methane emission fluxes from the Permian Basin for 2019–2020, **(b)** PDF of the Permian Basin emission fluxes for 2019–2020, **(c)** Annual mean methane emission fluxes from the Permian Basin after filtration in 2019–2020, **(d)** PDF of the 2019–2020 methane emission fluxes from the Permian Basin after filtration. Backgrounds of **(a)**, **(c)** are from Esri World Imagery | Powered by Esri.

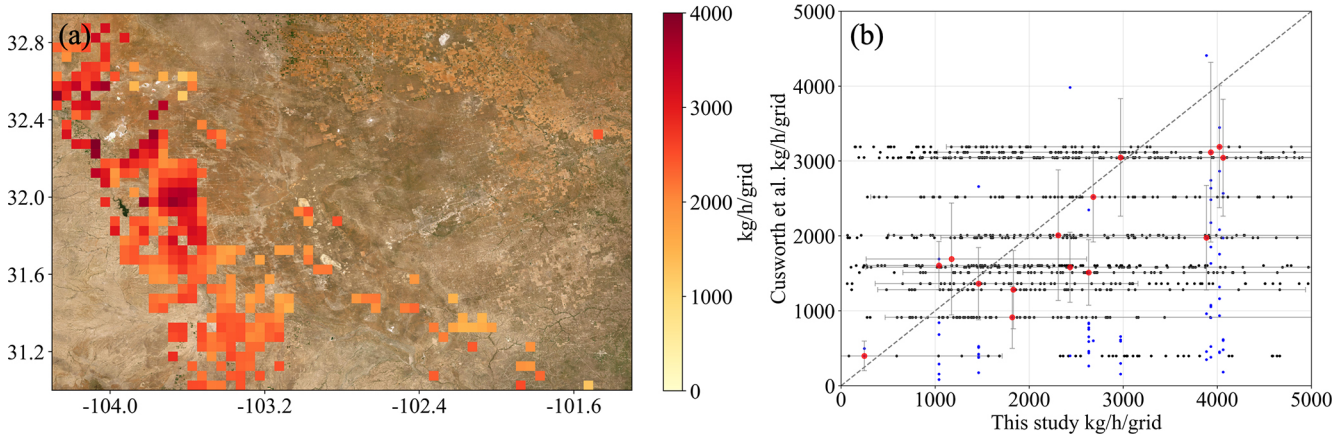

Figure 8. **(a)** Annual mean CH_4 emissions ($kg\,h^{-1}\,grid^{-1}$) on grids which overlap spatially with an emission observed by observed by Cusworth et al. (2021); **(b)** The red dots in the scatter plot represent the points where our valid emissions grids overlap in space and time with those of Cusworth et al. (2021). The black and blue dots denote emission estimates from our study on the same grids as observed by Cusworth et al. (2021), but observed by TROPOMI on different days, representing temporal variation. The gray error bars represent the associated uncertainties. The background of **(a)** is from Esri World Imagery | Powered by Esri.

sent our effective emissions and the emission estimates of Cusworth et al. (2021) on the same grid, but during other days when Cusworth et al. (2021) does not have observations but TROPOMI does. We found that the methane emissions from these emission facilities varied significantly over time, indicating that TROPOMI allows for a better understanding of how emissions dynamics may change over time.

4 Conclusion

This work used a mass conserving partial differential equation, with terms trained based on observations of CH_4 emissions from Changzhi, Shanxi, to compute emissions of CH_4 using daily and grid-by-grid TROPOMI X_{CH_4}, explicit uncertainty of retrieved X_{CH_4}, and reanalysis meteorological data, over and around the relatively clean area around the long-term WMO CH_4 background observation station at Waliguan and the heavily emitting CH_4 region of the Permian Basin. Inclusion of uncertainty in retrieved TROPOMI X_{CH_4} values are used to recompute emissions in a manner that considers the physically relevant non-linear effects of gradient calculation. The work further introduced an unbiased two-step filtering method, which effectively removes all negative values as well as both small and larger uncertain values in an unbiased manner, yielding results which are realistic and match well with underlying driving factors.

In Waliguan region we have identified CH_4 emissions, with a range from 0.3–187 $\mu g\,m^{-2}\,s^{-1}$, and validated that all resulting points are all locations containing known anthropogenic CH_4 source activities. The minimum inverted emission value ranges from 0.4–0.5 $\mu g\,m^{-2}\,s^{-1}$, depending on the amount of TROPOMI uncertainty applied. Due to our model's consideration of both the wind times concentration gradient and second order concentration gradient terms and actively propagates the TROPOMI data uncertainty, requiring a buffering from the linear and temporal derivative terms, a factor overlooked either in the name of model simplification or over-stiffness. When following the typical approach of removing negative emissions or using absolute values, excessive noise near 0 $\mu g\,m^{-2}\,s^{-1}$ obscures the true signal, while noisy but large values allow points to enter into the solution space which are also too large to be realistic.

To further validate our approach and results, we compared our emission rates computed over the Permian Basis with aircraft imaging spectrometers estimated by Cusworth et al. (2021). Our observations span a longer time series than Cusworth et al. (2021) (more temporally representative) and that the per-grid area is also larger than Cusworth et al. (2021) (per grid possibility of missed sources. This highlights the robustness of our method in capturing both smaller than currently considered possible emissions signals using TROPOMI, as well as reducing some amount of very large emission signals, which likely are a result of TROPOMI inversion noise on the positive side.

This work identifies three weaknesses to be addressed by future work. First, there is need to more carefully consider the inversions of multiple retrieved species in tandem, not just a single species, since other species may impact the inversion of CH_4. Second, future satellite missions which are capable of retrieving X_{CH_4} at a slightly higher spatial resolution than TROPOMI may yield additional gains. Third, the use of additional platforms that can yield more precise X_{CH_4} calculations will improve the ability to detect not only more signals, but to widen the possible detection range. Furthermore, there is the issue that the work herein is not reproducing a large number of very small emissions values, as claimed by some works (Chen et al., 2025), although the results seem to have a lower detection threshold than other TROPOMI based works (Cusworth et al., 2022).

In summary, our method provides a reliable framework for quantifying CH_4 emissions by effectively distinguishing genuine emission signals from noise, rigorously accounting for observational uncertainties, and validating results against independent datasets. This represents a significant advancement over traditional approaches, enabling more precise identification and quantification of CH_4 sources. Importantly, studies relying on TROPOMI or other satellite data that fail to actively incorporate observational uncertainties often underestimate true emissions on a grid-by-grid basis while simultaneously overestimating the number of emitting grids. This underscores the critical need to integrate uncertainty propagation into emission quantification methodologies to achieve robust and reliable results.

Data availability. The TROPOMI XCH_4 data can be found here: https://browser.dataspace.copernicus.eu/ (last access: January 2026). Daily ground station CH_4 data for Waliguan are obtained World Data Centre for Greenhouse: https://gaw.kishou.go.jp/search/file/0013-2015-1002-01-01-9999 (last access: 10 October 2025). The wind Gases data were obtained from the European Centre for Medium-Range Weather Forecasts ERA-5 reanalysis product (https://doi.org/10.24381/cds.bd0915c6, Hersbach et al., 2023). The ground measurement data and coefficients of Changzhi coal mine were obtained from Hu (2024). The point coordinates and emission rates of surface emission sources in the Permian Basin were obtained from Cusworth et al. (2021). The AAOD product used in this study is from (Multi-angle Imaging SpectroRadiometer) MISR satellite observations and are obtained from the NASA Langley Atmospheric Science Data Center (https://doi.org/10.5067/Terra/MISR/MIL3MAEN_L3.004, NASA/LARC/SD/ASDC, 2008). The satellite base maps used in this work are all from Esri World Imagery. All emissions computed in this work are available for download at https://doi.org/10.6084/m9.figshare.30635951 (Zheng et al., 2025).

Supplement. The supplement related to this article is available online at https://doi.org/10.5194/acp-26-1931-2026-supplement.

Author contributions. This work was conceptualized by JBC and BZ. The methods were developed by JBC and KQ. LL, WH, PT, SL, AG and HS provided insights on methodology. Investigation was done by BZ, JBC and KQ. Visualizations were made by BZ and JBC. Writing of the original draft was done by BZ and JBC. Writing at the review and editing stages were done by BZ and JBC.

Competing interests. The contact author has declared that none of the authors has any competing interests.

Disclaimer. Publisher's note: Copernicus Publications remains neutral with regard to jurisdictional claims made in the text, published maps, institutional affiliations, or any other geographical representation in this paper. The authors bear the ultimate responsibility for providing appropriate place names. Views expressed in the text are those of the authors and do not necessarily reflect the views of the publisher.

Acknowledgements. This study was funded by the International Science and Technology Cooperation Program of Jiangsu Province (BZ2024060). The satellite base map used in this study is from Esri World Imagery | Powered by Esri. These images are used strictly for academic, non-commercial research, in accordance with the fair use policy and in accordance with Eris' Terms of Service.

Financial support. This work was supported by the Natural Science Foundation of Jiangsu Province (grant no. BZ2024060).

Review statement. This paper was edited by Eduardo Landulfo and reviewed by Ge Han, Sang Seo Park, and two anonymous referees.

References

Balasus, N., Jacob, D. J., Lorente, A., Maasakkers, J. D., Parker, R. J., Boesch, H., Chen, Z., Kelp, M. M., Nesser, H., and Varon, D. J.: A blended TROPOMI + GOSAT satellite data product for atmospheric methane using machine learning to correct retrieval biases, Atmos. Meas. Tech., 16, 3787–3807, https://doi.org/10.5194/amt-16-3787-2023, 2023.

Boersma, K. F., Eskes, H. J., Richter, A., De Smedt, I., Lorente, A., Beirle, S., van Geffen, J. H. G. M., Zara, M., Peters, E., Van Roozendael, M., Wagner, T., Maasakkers, J. D., van der A, R. J., Nightingale, J., De Rudder, A., Irie, H., Pinardi, G., Lambert, J.-C., and Compernolle, S. C.: Improving algorithms and uncertainty estimates for satellite NO_2 retrievals: results from the quality assurance for the essential climate variables (QA4ECV) project, Atmos. Meas. Tech., 11, 6651–6678, https://doi.org/10.5194/amt-11-6651-2018, 2018.

Chen, C., Dubovik, O., Schuster, G. L., Chin, Mian., Henze, D. K., Lapyonok, T., Li, Z., Derimian, Y., and Zhang, Y.: Multi-angular polarimetric remote sensing to pinpoint global aerosol absorption and direct radiative forcing, Nat. Commun., 13, 7459, https://doi.org/10.1038/s41467-022-35147-y, 2022.

Chen, L., Song, Z., Yao, N., Xi, H., Li, J., Gao, P., Chen, Y., Su, H., Sun, Y., Jiang, B., Chen, J., Zhang, Y., Zhu, Y., Li, P., Pang, X., and Yu, S.: Photostationary state assumption seriously underestimates NO_x emissions near large point sources at 10 to 60 m pixel resolution, Proc. Natl. Acad. Sci, 122, e2423915122, https://doi.org/10.1073/pnas.2423915122, 2025.

Cohen, J. B. and Prinn, R. G.: Development of a fast, urban chemistry metamodel for inclusion in global models, Atmos. Chem. Phys., 11, 7629–7656, https://doi.org/10.5194/acp-11-7629-2011, 2011.

Cohen, J. B., Prinn, R. G., and Wang, C.: The impact of detailed urban-scale processing on the composition, distribution, and radiative forcing of anthropogenic aerosols, Geophys. Res. Lett., 38, L10808, https://doi.org/10.1029/2011GL047417, 2011.

Crippa, M., Guizzardi, D., Pagani, F., Schiavina, M., Melchiorri, M., Pisoni, E., Graziosi, F., Muntean, M., Maes, J., Dijkstra, L., Van Damme, M., Clarisse, L., and Coheur, P.: Insights into the spatial distribution of global, national, and subnational greenhouse gas emissions in the Emissions Database for Global Atmospheric Research (EDGAR v8.0), Earth Syst. Sci. Data, 16, 2811–2830, https://doi.org/10.5194/essd-16-2811-2024, 2024.

Cusworth, D. H., Duren, R. M., Thorpe, A. K., Olson-Duvall, W., Heckler, J., Chapman, J. W., Eastwood, M. L., Helmlinger, M. C., Green, R. O., Asner, G. P., Dennison, P. E., and Miller, C. E.: Intermittency of Large Methane Emitters in the Permian Basin, Environ. Sci. Technol. Lett, 8, 7, 567–573, https://doi.org/10.1021/acs.estlett.1c00173, 2021.

Cusworth, D. H., Thorpe, A. T., Ayasse, A. K., Stepp, D., Heckler, J., Asner, G. P., Miller, C. E., Yadav, V., Chapman, J. 2., Eastwood, M. L., Green, R. O., Hmiel, B., Lyon, D. R., and Duren, R. M.: Strong methane point sources contribute a disproportionate fraction of total emissions across multiple basins in the United States, Proc. Natl. Acad. Sci, 119, e2202338119, https://doi.org/10.1073/pnas.2202338119, 2022.

Erland, B. M., Thorpe, A. K., and Gamon, J. A.: Recent Advances Toward Transparent Methane Emissions Monitoring: A Review, Environ. Sci. Technol., 56, 16567–16581, https://doi.org/10.1021/acs.est.2c02136, 2022.

Frankenberg, C., Meirink, J. F., Weele, M. V., Platt, U., and Wagner, T.: Assessing Methane Emissions from Global Space-Borne Observations, Science, 308, 1010–1014, https://doi.org/10.1126/science.1106644, 2005.

Frankenberg, C., Thorpe, A. K., Thompson, D. R., Hulley, G., Kort, E. A., Vance, N., Borchardt, J., Krings, T., Gerilowski, K., Sweeney, C., Conley, S., Bue, B. D., Aubrey, A. D., Hook, S., and Green, R. O.: Airborne methane remote measurements reveal heavy-tail flux distribution in Four Corners region, Proc. Natl. Acad. Sci., 113, 9734–9739, https://doi.org/10.1073/pnas.1605617113, 2016.

Gao, M., Xing, Z., Vollrath, C., Hugenholtz, C. H., and Barchyn, T. E.: Global observational coverage of onshore oil and gas methane sources with TROPOMI, Sci. Rep.-UK, 13, 16759, https://doi.org/10.1038/s41598-023-41914-8, 2023.

Gaubert, B., Arellano Jr., A. F., Barré, J., Worden, H. M., Emmons, L. K., Tilmes, S., Buchholz, R. R., Vitt, F., Raeder, K., Collins, N., Anderson, J. L., Wiedinmyer, C., Martinez Alonso, S., Edwards, D. P., Andreae, M. O., Hannigan, J. W., Petri, C., Strong, K., and Jones, N.: Toward a chemical reanalysis in a coupled chemistry-climate model: An evaluation of MOPITT CO assimilation and its impact on tropospheric composition, J. Geophys. Res. Atmos, 121, 7310–7343, https://doi.org/10.1002/2016JD024863, 2016.

Gaubert, B., Worden, H. M., Arellano, A. F. J., Emmons, L. K., Tilmes, S., Barré, J., Martinez Alonso, S., Vitt, F., Anderson, J. L., Alkemade, F., Houweling, S., and Ed-

wards, D. P.: Chemical feedback from decreasing carbon monoxide emissions, Geophys. Res. Lett., 44, 9985–9995, https://doi.org/10.1002/2017GL074987, 2017.

Hachmeister, J., Schneising, O., Buchwitz, M., Lorente, A., Borsdorff, T., Burrows, J. P., Notholt, J., and Buschmann, M.: On the influence of underlying elevation data on Sentinel-5 Precursor TROPOMI satellite methane retrievals over Greenland, Atmos. Meas. Tech., 15, 4063–4074, https://doi.org/10.5194/amt-15-4063-2022, 2022.

Hancock, S. E., Jacob, D. J., Chen, Z., Nesser, H., Davitt, A., Varon, D. J., Sulprizio, M. P., Balasus, N., Estrada, L. A., Cazorla, M., Dawidowski, L., Diez, S., East, J. D., Penn, E., Randles, C. A., Worden, J., Aben, I., Parker, R. J., and Maasakkers, J. D.: Satellite quantification of methane emissions from South American countries: a high-resolution inversion of TROPOMI and GOSAT observations, Atmos. Chem. Phys., 25, 797–817, https://doi.org/10.5194/acp-25-797-2025, 2025.

He, Q., Qin, K., Cohen, J. B., Li, D., and Kim, J.: Quantifying Uncertainty in ML-derived Atmosphere Remote Sensing: Hourly Surface NO_2 Estimation with GEMS, Geophys. Res. Lett., 18, e2024GL110468, 2024.

Hemati, M., Mahdianpari, M., Nassar, R., Shiri, H., and Mohammadimanesh, F.: Urban methane emission monitoring across North America using TROPOMI data: an analytical inversion approach, Sci. Rep.-UK, 14, 9041, https://doi.org/10.1038/s41598-024-58995-8, 2024.

Hersbach, H., Bell, B., Berrisford, P., Biavati, G., Horányi, A., Muñoz Sabater, J., Nicolas, J., Peubey, C., Radu, R., Rozum, I., Schepers, D., Simmons, A., Soci, C., Dee, D., and Thépaut, J.-N.: ERA5 hourly data on pressure levels from 1940 to present, Copernicus Climate Change Service (C3S) Climate Data Store (CDS) [data set], https://doi.org/10.24381/cds.bd0915c6, 2023.

Hu, H., Hasekamp, O., Butz, A., Galli, A., Landgraf, J., Aan de Brugh, J., Borsdorff, T., Scheepmaker, R., and Aben, I.: The operational methane retrieval algorithm for TROPOMI, Atmos. Meas. Tech., 9, 5423–5440, https://doi.org/10.5194/amt-9-5423-2016, 2016.

Hu, H., Landgraf, J., Detmers, R., Borsdorff, T., Aan De Brugh, J., Aben, I., Butz, A., and Hasekamp, O.: Toward global mapping of methane with TROPOMI: First results and intersatellite comparison to GOSAT, Geophys. Res. Lett., 45, 3682–3689, https://doi.org/10.1002/2018GL077259, 2018.

Hu, W., Qin, K., Lu, F., Li, D., and Cohen, J. B.: Merging TROPOMI and eddy covariance observations to quantify 5 years of daily CH_4 emissions over coal-mine dominated region, Int. J. Coal Sci. Technol., 11, 56, https://doi.org/10.1007/s40789-024-00700-1, 2024.

Kahn, R. A., Andrews, E., Brock, C. A., Chin, M., Feingold, G., Gettelman, A., Levy, R. C., Murphy, D. M., Nenes, A., Pierce, J. R., Popp, T., Redemann, J., Sayer, A. M., da Silva, A. M., Sogacheva, L., and Stier, P.: Reducing Aerosol Forcing Uncertainty by Combining Models With Satellite and Within-The-Atmosphere Observations: A Three-Way Street, Rev. Geophys., 61, e2022RG000796, https://doi.org/10.1029/2022RG000796, 2023.

Kuhlmann, G., Stavropoulou, F., Schwietzke, S., Zavala-Araiza, D., Thorpe, A., Hueni, A., Emmenegger, L., Calcan, A., Röckmann, T., and Brunner, D.: Evidence of successful methane mitigation in one of Europe's most important oil production region, Atmos. Chem. Phys., 25, 5371–5385, https://doi.org/10.5194/acp-25-5371-2025, 2025.

Li, K., Bai, K., Jiao, P., Chen, H., He, H., Shao, L., Sun, Y., Zheng, Z., Li, R., and Chang, N.: Developing unbiased estimation of atmospheric methane via machine learning and multiobjective programming based on TROPOMI and GOSAT data, Remote Sens. Environ., 304, 114039, https://doi.org/10.1016/j.rse.2024.114039, 2024.

Li, X., Cohen, J. B., Qin, K., Geng, H., Wu, X., Wu, L., Yang, C., Zhang, R., and Zhang, L.: Remotely sensed and surface measurement- derived mass-conserving inversion of daily NO_x emissions and inferred combustion technologies in energy-rich northern China, Atmos. Chem. Phys., 23, 8001–8019, https://doi.org/10.5194/acp-23-8001-2023, 2023.

Li, X., Cohen, J. B., Tiwari, P., Wu, L., Wang, S., He, Q., Yang, H and Qin, K.: Space-based inversion reveals underestimated carbon monoxide emissions over Shanxi, Commun. Earth Environment, 6, 357, https://doi.org/10.1038/s43247-025-02301-5, 2025.

Liang, R., Zhang, Y., Chen, W., Zhang, P., Liu, J., Chen, C., Mao, H., Shen, G., Qu, Z., Chen, Z., Zhou, M., Wang, P., Parker, R. J., Boesch, H., Lorente, A., Maasakkers, J. D., and Aben, I.: East Asian methane emissions inferred from high-resolution inversions of GOSAT and TROPOMI observations: a comparative and evaluative analysis, Atmos. Chem. Phys., 23, 8039–8057, https://doi.org/10.5194/acp-23-8039-2023, 2023.

Liu, J., Cohen, J. B., He, Q., Tiwari, P., and Qin, K.: Accounting for NO_x emissions from biomass burning and urbanization doubles existing inventories over South, Southeast and East Asia, Communications Earth and Environment, 5, 255, https://doi.org/10.1038/s43247-024-01424-5, 2024a.

Liu, J., Cohen, J. B., Tiwari, P., Liu, Z., Yim, S. H. L., Gupta, P., and Qin, K.: New top-down estimation of daily mass and number column density of black carbon driven by OMI and AERONET observations, Remote Sens. Environ., 315, 114436, https://doi.org/10.1016/j.rse.2024.114436, 2024b.

Liu, M., van der A, R., van Weele, M., Bryan, L., Eskes, H., Veefkind, P., Liu, Y., Lin, X., de Laat, J., and Ding, J.: Current potential of CH_4 emission estimates using TROPOMI in the Middle East, Atmos. Meas. Tech., 17, 5261–5277, https://doi.org/10.5194/amt-17-5261-2024, 2024a.

Liu, M., van der A, R., van Weele, M., Eskes, H., Lu, X., Veefkind, P., de Laat, J., Kong, H., Wang, J., Sun, J., Ding, J., Zhao, Y., and Weng, H.: A New Divergence Method to Quantify Methane Emissions Using Observations of Sentinel-5P TROPOMI, Geophys. Res. Lett., 48, e2021GL094151, https://doi.org/10.1029/2021GL094151, 2021.

Liu, S., Fang, S., Liu, P., Liang, M., Guo, M., and Feng, Z.: Measurement report: Changing characteristics of atmospheric CH_4 in the Tibetan Plateau: records from 1994 to 2019 at the Mount Waliguan station, Atmos. Chem. Phys., 21, 393–413, https://doi.org/10.5194/acp-21-393-2021, 2021.

Liu, Z., Cohen, J. B., Tiwari, P., Guan, L., Wang, S., Li, Z., and Qin, K.: A global black carbon dataset of column concentration and microphysical information derived from MISR multi-band observations and Mie scattering simulations, Earth Syst. Sci. Data, 18, 507–533, https://doi.org/10.5194/essd-18-507-2026, 2026.

Liu, Z., Cohen, J. B., Wang, S., Wang, X., Tiwari, P., and Qin, K.: Remotely sensed BC columns over rapidly changing Western China show significant decreases in mass and inconsistent changes in number, size, and mixing properties due to policy actions, npj Clim. Atmos. Sci., 7, 124, https://doi.org/10.1038/s41612-024-00663-9, 2024b.

Lorente, A., Borsdorff, T., Butz, A., Hasekamp, O., aan de Brugh, J., Schneider, A., Wu, L., Hase, F., Kivi, R., Wunch, D., Pollard, D. F., Shiomi, K., Deutscher, N. M., Velazco, V. A., Roehl, C. M., Wennberg, P. O., Warneke, T., and Landgraf, J.: Methane retrieved from TROPOMI: improvement of the data product and validation of the first 2 years of measurements, Atmos. Meas. Tech., 14, 665–684, https://doi.org/10.5194/amt-14-665-2021, 2021.

NASA/LARC/SD/ASDC: MISR Level 3 Component Global Aerosol product in netCDF format covering a month V004, ASDC [data set], https://doi.org/10.5067/Terra/MISR/MIL3MAEN_L3.004, 2008.

Nesser, H., Jacob, D. J., Maasakkers, J. D., Lorente, A., Chen, Z., Lu, X., Shen, L., Qu, Z., Sulprizio, M. P., Winter, M., Ma, S., Bloom, A. A., Worden, J. R., Stavins, R. N., and Randles, C. A.: High-resolution US methane emissions inferred from an inversion of 2019 TROPOMI satellite data: contributions from individual states, urban areas, and landfills, Atmos. Chem. Phys., 24, 5069–5091, https://doi.org/10.5194/acp-24-5069-2024, 2024.

Parker, P., Boesch, H., Cogan, A., Fraser, A., Feng, L., Palmer, P. I., Messerschmidt, J., Deutscher, N., Griffith, D. W. T., Notholt, J., Wennberg, P. O., and Wuch, D.: Methane observations from the Greenhouse Gases Observing SATellite: Comparison to ground-based TCCON data and model calculations, Geophys. Res. Lett., 38, https://doi.org/10.1029/2011GL047871, 2011.

Pollard, D. F., Hase, F., Sha, M. K., Dubravica, D., Alberti, C., and Smale, D.: Retrievals of X_{CO_2}, X_{CH_4} and X_{CO} from portable, near-infrared Fourier transform spectrometer solar observations in Antarctica, Earth Syst. Sci. Data, 14, 5427–5437, https://doi.org/10.5194/essd-14-5427-2022, 2022.

Prinn, R. G., Huang, J., Weiss, R. F., Cunnold, D. M., Fraser, P. J., Simmonds, P. G., Mcculloch, A., Harth, C., Salameh, P., O'doherty, S., Wang, R. H. J., Porter, L., and Miller, B. R.: Evidence for Substantial Variations of Atmospheric Hydroxyl Radicals in the Past Two Decades, Science, 292, 1882–1888, https://doi.org/10.1126/science.1058673, 2001.

Qin, K., Lu, L., Liu, J., He, Q., Shi, J., Deng, W., Wang, S., and Cohen, J. B.: Model-free daily inversion of NO_x emissions using TROPOMI (MCMFE-NO_x) and its uncertainty: Declining regulated emissions and growth of new sources, Remote Sens. Environ., 295, 113720, https://doi.org/10.1016/j.rse.2023.113720, 2023.

Qu, Z., Jacob, D. J., Shen, L., Lu, X., Zhang, Y., Scarpelli, T. R., Nesser, H., Sulprizio, M. P., Maasakkers, J. D., Bloom, A. A., Worden, J. R., Parker, R. J., and Delgado, A. L.: Global distribution of methane emissions: a comparative inverse analysis of observations from the TROPOMI and GOSAT satellite instruments, Atmos. Chem. Phys., 21, 14159–14175, https://doi.org/10.5194/acp-21-14159-2021, 2021.

Sadavarte, P., Pandey, S., Maasakkers, J. D., Lorente, A., Borsdorff, T., van der Gon, H. D., Houweling, S., and Aben, I.: Methane Emissions from Superemitting Coal Mines in Australia Quantified Using TROPOMI Satellite Observations, Environ. Sci. Technol, 55, 24, 16573–16580, https://doi.org/10.1021/acs.est.1c03976, 2021.

Schneising, O., Buchwitz, M., Hachmeister, J., Vanselow, S., Reuter, M., Buschmann, M., Bovensmann, H., and Burrows, J. P.: Advances in retrieving XCH_4 and XCO from Sentinel-5 Precursor: improvements in the scientific TROPOMI/WFMD algorithm, Atmos. Meas. Tech., 16, 669–694, https://doi.org/10.5194/amt-16-669-2023, 2023.

Schneising, O., Buchwitz, M., Reuter, M., Vanselow, S., Bovensmann, H., and Burrows, J. P.: Remote sensing of methane leakage from natural gas and petroleum systems revisited, Atmos. Chem. Phys., 20, 9169–9182, https://doi.org/10.5194/acp-20-9169-2020, 2020.

Sha, M. K., Langerock, B., Blavier, J.-F. L., Blumenstock, T., Borsdorff, T., Buschmann, M., Dehn, A., De Mazière, M., Deutscher, N. M., Feist, D. G., García, O. E., Griffith, D. W. T., Grutter, M., Hannigan, J. W., Hase, F., Heikkinen, P., Hermans, C., Iraci, L. T., Jeseck, P., Jones, N., Kivi, R., Kumps, N., Landgraf, J., Lorente, A., Mahieu, E., Makarova, M. V., Mellqvist, J., Metzger, J.-M., Morino, I., Nagahama, T., Notholt, J., Ohyama, H., Ortega, I., Palm, M., Petri, C., Pollard, D. F., Rettinger, M., Robinson, J., Roche, S., Roehl, C. M., Röhling, A. N., Rousogenous, C., Schneider, M., Shiomi, K., Smale, D., Stremme, W., Strong, K., Sussmann, R., Té, Y., Uchino, O., Velazco, V. A., Vigouroux, C., Vrekoussis, M., Wang, P., Warneke, T., Wizenberg, T., Wunch, D., Yamanouchi, S., Yang, Y., and Zhou, M.: Validation of methane and carbon monoxide from Sentinel-5 Precursor using TCCON and NDACC-IRWG stations, Atmos. Meas. Tech., 14, 6249–6304, https://doi.org/10.5194/amt-14-6249-2021, 2021.

Tao, M., Cai, Z., Zhu, S., Liu, Y., Feng, L., Fang, S., Yi, Y., and Bian, J.: New evidence for CH_4 enhancement in the upper troposphere associated with the Asian summer monsoon, Environ. Res. Lett., 19, 034033, https://doi.org/10.1088/1748-9326/ad2738, 2024.

Tian, X., Wang, Y., Beirle, S., Xie, P., Wagner, T., Xu, J., Li, A., Dörner, S., Ren, B., and Li, X.: Technical note: Evaluation of profile retrievals of aerosols and trace gases for MAX-DOAS measurements under different aerosol scenarios based on radiative transfer simulations, Atmos. Chem. Phys., 21, 12867–12894, https://doi.org/10.5194/acp-21-12867-2021, 2021.

Tiwari, P., Cohen, J. B., Lu, L., Wang, S., Li, X., Guan, L., Liu, Z., Li, Z., and Qin, K.: Multi-platform observations and constraints reveal overlooked urban sources of black car bon in Xuzhou and Dhaka, Commun. Earth. Environ, 6, 38, https://doi.org/10.1038/s43247-025-02012-x, 2025.

Tiwari, P., Cohen, J. B., Wang, X., Wang, S., and Qin, K.: Radiative forcing bias calculation based on COSMO (Core-Shell Mie model Optimization) and AERONET data, npj Clim. Atmos. Sci., 6, 193, https://doi.org/10.1038/s41612-023-00520-1, 2023.

Torres, O., Jethva, H., Ahn, C., Jaross, G., and Loyola, D. G.: TROPOMI aerosol products: evaluation and observations of synoptic-scale carbonaceous aerosol plumes during 2018–2020, Atmos. Meas. Tech., 13, 6789–6806, https://doi.org/10.5194/amt-13-6789-2020, 2020.

Vanselow, S., Schneising, O., Buchwitz, M., Reuter, M., Bovensmann, H., Boesch, H., and Burrows, J. P.: Automated detection of regions with persistently enhanced methane concentrations using Sentinel-5 Precursor satellite data, Atmos. Chem.

Phys., 24, 10441–10473, https://doi.org/10.5194/acp-24-10441-2024, 2024.

Varon, D. J., Jacob, D. J., Estrada, L. A., Balasus, N., East, J., Pendergrass, D. C., Chen, Z., Sulprizio, M., Omara, M., Gautam, R., Barkley, Z. R., Cardoso Saldaña, F. J., Reidy, E. K., Kamdar, H., Sherwin, E. D., Biraud, S. C., Jervis, D., Pandey, S., Worden, J. R., Bowman, K, W., Maasakkers, J. D., and Kleinberg, R. L.: Seasonality and Declining Intensity of Methane Emissions from the Permian and Nearby US Oil and Gas Basins, Environmental Science & Technology, 60, 425–435, https://doi.org/10.1021/acs.est.5c08745, 2025.

Varon, D. J., Jacob, D. J., Hmiel, B., Gautam, R., Lyon, D. R., Omara, M., Sulprizio, M., Shen, L., Pendergrass, D., Nesser, H., Qu, Z., Barkley, Z. R., Miles, N. L., Richardson, S. J., Davis, K. J., Pandey, S., Lu, X., Lorente, A., Borsdorff, T., Maasakkers, J. D., and Aben, I.: Continuous weekly monitoring of methane emissions from the Permian Basin by inversion of TROPOMI satellite observations, Atmos. Chem. Phys., 23, 7503–7520, https://doi.org/10.5194/acp-23-7503-2023, 2023.

Veefkind, J. P., Serrano-Calvo, R., de Gouw, J., Dix, B., Schneising, O., Buchwitz, M., Barré, J., van der A, R. J., Liu, M., and Levelt, P. F.: Widespread frequent methane emissions from the oil and gas industry in the Permian basin, J. Geophys. Res.-Atmospheres, 128, e2022JD037479, https://doi.org/10.1029/2022JD037479, 2023.

Vignati, E., Karl, M., Krol, M., Wilson, J., Stier, P., and Cavalli, F.: Sources of uncertainties in modelling black carbon at the global scale, Atmos. Chem. Phys., 10, 2595–2611, https://doi.org/10.5194/acp-10-2595-2010, 2010.

Wang, S., Cohen, J. B., Guan, L., Lu, L., Tiwari, P., and Qin, K.: Observationally constrained global NO_x and CO emissions variability reveals sources which contribute significantly to CO_2 emissions, npj Clim. Atmos. Sci., 8, 87, https://doi.org/10.1038/s41612-025-00977-2, 2025.

Webb, E. K., Pearman, G. I., and Leuning, R.: Correction of flux measurements for density effects due to heat and water vapour transfer, Q. J. Roy. Meteor. Soc., 106, 85–100, https://doi.org/10.1002/qj.49710644707, 1980.

Yang, G., Zheng, Z., Abbott, B. W., Olefeldt, D., Knoblauch, C., Song, Y., Kang, L., Qin, S., Peng, Y., and Yang, Y.: Characteristics of methane emissions from alpine thermokarst lakes on the Tibetan Plateau, Nat. Commun., 14, 3121, https://doi.org/10.1038/s41467-023-38907-6, 2023.

Yu, X., Millet, D. B., Henze, D. K., Turner, A. J., Delgado, A. L., Bloom, A. A., and Sheng, J.: A high-resolution satellite-based map of global methane emissions reveals missing wetland, fossil fuel, and monsoon sources, Atmos. Chem. Phys., 23, 3325–3346, https://doi.org/10.5194/acp-23-3325-2023, 2023.

Zhang, L., Xia, X., Liu, S., Zhang, S., Li, S., Wang, J., Wang, G., Gao, H., Zhang, Z., Wang, Q., Wen, W., Liu, R., Yang, Z., Stanley, E. H., and Raymond, P. A.: Significant methane ebullition from alpine permafrost rivers on the East Qinghai–Tibet Plateau, Nat. Geosci., 13, 349–354, https://doi.org/10.1038/s41561-020-0571-8, 2020.

Zheng, B., Cohen, J. B., Lu, L., Hu, W., Tiwari, P., Lolli, S., Garzelli, A., Su, H., and Qin, K.: How can we trust TROPOMI based Methane Emissions Estimation: Calculating Emissions over Unidentified Source Regions, Figshare [data set], https://doi.org/10.6084/m9.figshare.30635951, 2025.

Zhou, L., Worthy, D. E. J., Lang, P. M., Ernst, M. K., Zhang, X. C., Wen, Y. P., and Li, J. L.: Ten years of atmospheric methane observations at a high elevation site in Western China, Atmos. Environ., 38, 7040–7054, https://doi.org/10.1016/j.atmosenv.2004.02.072, 2004.